Gliding arc/glow discharge for CO_2 conversion: Comparing the performance of different discharge configurations

V Ivanov[a,*], Ts Paunska[a], S Lazarova[a], A Bogaerts[b], and St Kolev[a,*]

[a]Faculty of Physics, Sofia University, 5 James Bourchier Boulevard, 1164 Sofia, Bulgaria
[b]Research group PLASMANT, Department of Chemistry, University of Antwerp, Universiteitsplein 1, BE-2610 Antwerp, Belgium
[*]Corresponding authors: vladislavvi@phys.uni-sofia.bg (V. Ivanov), skolev@phys.uni-sofia.bg (St. Kolev)

Abstract

We studied the use of low current (hundreds of milliamperes) gliding arc/glow discharges for CO_2 dissociation, at atmospheric pressure, in three different configurations. All of these are based on the gliding arc design with flat diverging electrodes. The discharge is mainly in the normal glow regime with contracted positive column. The CO_2 gas is injected from a nozzle, at the closest separation between the electrodes. A pair of quartz glasses is placed on both sides of the electrodes, so that the gas flow is restricted to the active plasma area, between the electrodes. For two of the tested configurations, an external magnetic field was applied, to create a magnetic force, both in the direction of the gas flow, and opposite to the gas flow. In the first case, the arc is accelerated, shortening the period between ignition and extinction, while in the second case, it is stabilized (magnetically-stabilized). We studied two quantities, namely the CO_2 conversion and the energy efficiency of the conversion. Generally, the CO_2 conversion decreases with increasing flow rate and increases with power. The energy efficiency increases with the flow rate, for all configurations. The magnetically-stabilized configuration is more stable and efficient at low gas flow rates, but has poor performance at high flow rates, while the non-stabilized configurations exhibit good conversion for a larger range of flow rates, but they are generally more unstable and less efficient.

Keywords

CO_2 conversion, CO_2 dissociation, low current gliding arc, magnetic stabilization, magnetically stabilized discharge, gliding glow discharge

1 Introduction

The direct conversion of CO_2 to CO and O_2 is of particular interest to researchers and the industry. For example, the product of this reaction – CO, can be used for methanol production. Through the process $CO + 2H_2 \rightarrow CH_3OH$, complete conversion to methanol can be achieved. This is a better alternative to the direct CO_2 hydrogenation approach ($CO_2 + 3H_2 \rightarrow CH_3OH + H_2O$), as in the latter case a third of the hydrogen is converted into water.

The traditional process of direct dissociation of CO_2 into O_2 and CO, using heat, is very inefficient, because the CO_2 molecule is thermodynamically very stable. Thermal CO_2 dissociation involves heating of the gas to temperatures above 2000 K, and beyond 5000 K it is even possible to have full conversion [1]. At low temperatures, the reaction of thermal CO_2 splitting reaches its equilibrium, and at that point very little conversion is possible.

There is an ongoing search for a more efficient way to perform CO_2 dissociation. Several alternatives to thermal conversion have been investigated. These include solar thermochemical conversion, electrochemical conversion, biochemical conversion, plasma-assisted conversion and others [1, 2]. Some of these, like electrochemical and plasma-assisted conversion, target the renewable wind and solar energy sources, with the idea being to utilize the electrical power, generated during the time of low grid consumption.

Plasma-assisted conversion makes use of non-thermal or warm plasmas, which can operate at atmospheric pressure, and at low power. These and other characteristics make plasma conversion devices appealing, as their cost to construct and operate can be sufficiently small. In terms of efficiency, some of these, like gliding arc discharges for example, can even rival the efficiency of water electrolysis [1].

Non-thermal, or warm plasmas, are characterized by a sufficiently high electron density, with typical electron temperatures of several eV. At these values for the electron temperature, the CO_2 conversion is possible through direct electron impact dissociation ($CO_2 + e^- \rightarrow CO + O + e^-$), through dissociative electron attachment ($CO_2 + e^- \rightarrow CO + O^-$), or stepwise dissociation through the vibrationally excited CO_2 states. The vibrational stepwise dissociation is identified as an efficient channel for conversion [3, 4, 5], and is of a particular interest to the research of non-thermal conversion methods. However, the dominant dissociation pathway, at the conditions of a GA discharge at atmospheric pressure, is thermal dissociation. The optimal gas temperature for this process is between $3000 - 4000$ K [6].

Several non-thermal plasma types have been utilized for CO_2 conversion. These include dielectric barrier discharges (DBD) [7, 8, 9, 10], microwave (MW) plasmas [11, 12, 13, 14] and gliding arc (GA) discharges [15, 16, 17, 18, 19, 20]. Plasmas operating at atmospheric pressure are preferable, because they don't require an expensive vacuum system. DBDs can operate at atmospheric pressure, but have low energy efficiencies – below 20 %, which is caused by their inability to efficiently provide for the stepwise vibrational dissociation. MW discharges can allow for vibrational dissociation and can reach very high conversion (over 80 % [14]), but are efficient mainly at low pressures. GA discharges, commonly operate at atmospheric pressure and can reach efficiencies of $40 - 50$ %, as shown in [15, 19, 20, 21].

GA discharges are classically in a 2D diverging electrode configuration. The use of such devices for plasma-based CO_2 treatment is studied for instance in [15, 16, 17]. They have a relatively simple construction, and can operate in a variety of conditions, but also have some disadvantages. These are mainly related to their impractical shape, and debatably the low residence time, i.e. the gas has less time to interact with the plasma, and the low percentage of the treated gas [1]. A more sophisticated type of GA discharge has a 3D configuration, employing a vortex, or tornado flow [19, 20, 21], with variations including a magnetic field [18].

The aim of this study is to test the performance of three different 2D GA discharges for CO_2 dissociation. The first is of the basic GA discharge. In the second configuration, the arc glides with increased speed, because of the presence of an additional magnetic force, which is oriented in the same direction as the gas flow. In the third configuration, the arc is magnetically-stabilized by a magnetic field, which pushes it in a direction, opposite the gas flow. In this type of arrangement, the arc remains stabilized at a certain position along the electrodes and has a fixed length. The effect of magnetic arc stabilization was previously examined in [22]. The choice of this "2D GA" discharge allows for comparison of the magnetically stabilized and non-stabilized configuration which is hardly possible with other types of discharge configurations.

It is important to mention, that since our study suggests that the gliding discharge can operate in both arc and glow modes (see section 4.2), from this point on, we will use the more generic term

"Gliding Discharge" (GD) instead of "Gliding Arc" (GA).

The CO_2 gas enters the GD reactor from a nozzle, located at the closest distance between the electrodes. A pair of quartz glasses, placed on top of the electrodes, channel the gas flow, so that the inlet gas passes through the gap between the electrodes and through the arc.

We have calculated the CO_2 conversion, the specific energy input (SEI) and the energy efficiency, for the three different devices. The conversion is defined as the percentage of converted CO_2 gas, after plasma treatment. The energy efficiency is the ratio between the minimum required energy to achieve the measured conversion and the total energy provided to the device.

In section 2, we present a detailed overview of the entire experimental setup. This includes a description of the different types of discharge configurations, the construction of the discharge device, and the power supply used in our experiments, as well as the measurement process. Section 3 covers how the main quantities of interest are defined, and how their values and uncertainties are calculated. Section 4 focuses on the analysis of the experimental results and the behaviour of the discharge device. We make a comparison between the different discharge configurations, based on their conversion performance and energy efficiency. In section 5, we present our conclusions.

2 Experimental setup

An overall schematic of the experimental system is presented in figure 1. The central part of the system is the discharge device – figure 1(2). It is placed inside a sealed glass tube, which remains at atmospheric pressure at all time, as is the rest of the gas system. Inside the glass tube is where the actual gas treatment takes place. The flow of gas to the discharge device is controlled using mass-flow controllers (MFC: Bronkhorst EL-FLOW F-201CM) – figure 1(1). Power is provided from a custom-built high voltage power supply – figure 1(3). This power supply is described in more detail in section 2.2.

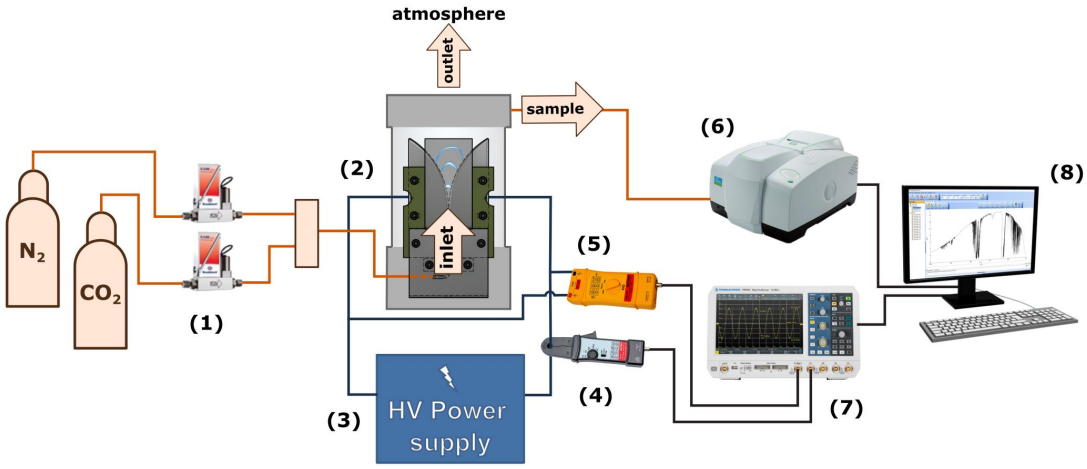

Figure 1: Schematic diagram of the components of the experimental system – Mass Flow Controllers (1), Discharge device (2), High voltage power supply (3), Current probe (4), High voltage probe (5), FT-IR Spectrometer (6), Oscilloscope (7), PC for data processing (8).

A single experimental measurement proceeds as follows. First, the gas inlet flow rate is adjusted from the mass flow controllers. The gas enters the glass tube from the inlet, and passes through the plasma discharge. The tube has an outlet connected to the outside atmosphere, so some of the treated gas escapes through this outlet, keeping the pressure inside the tube at 1 atm. It is safe to assume

that the concentration of CO_2 at the inlet is nearly 100 %, because the gas used in our experiments is rated to be with purity over 99.9 %.

The operating times for the discharge were determined from an additional series of measurements, and are dependent on the gas flow rate. They are chosen to be sufficiently long, to ensure that the CO_2 concentration has reached a steady state and no longer changes, and that processed gas mixture fills the entire gas system, including the glass tube and connecting pipes. This is needed since the gas sampling is not done directly at the discharge outlet, but from the containing glass chamber, which has a large volume. Once the system is filled with the converted gas, a sample of the gas mixture is extracted for analysis, after which the discharge is switched off. The processed gas, including the gas sample no longer interacts with the conversion device. The sample is fed into a Fourier Transform Infrared (FT-IR) spectrometer – figure 1(6). The FT-IR gas sample cell is a tube with a fixed volume, with two windows, made of CaF_2 glass. Its optical length is 10 cm and its diameter is 6 cm. Using the FT-IR, we measure the absorbance spectra of the gas sample. This absorbance is relative to a background (reference) measurement of a sample containing only CO_2. To calculate the conversion of the gas sample, we measure the absorbance value from a single line of the molecular band of the CO molecule, at 2209 cm^{-1}. The input CO_2 gas is of high enough purity (above 99.9 %) and we assume that it is basically converted to CO and O_2 with negligible amount of carbon C and ozone O_3. This is justified by the following: 1) No carbon deposition was observed in the systems and in the gas filters at the FTIR inlet, during the time it took to complete all experimental measurements (tens of hours). 2) The measured infrared spectra show no presence of O_3 absorption, within the limits of the apparatus sensitivity. In every experiment, we measure the spectrum in the range from 1000 to 6000 cm^{-1}, which includes infrared ozone absorption bands with significant cross sections. 3) In the literature, experiments using DBD discharges [7, 23], and gliding arc discharges [24] report negligible quantities of ozone, which was also supported by the results from numerical modelling [7, 24]. In [24], at similar conditions to ours, there is a study for both the plasma (arc phase) and the post discharge (relaxation phase), and it is shown that despite the increase of O_3 in the post discharge phase, it's concentration remains nearly two orders of magnitude lower than that of the O_2.

The conversion measurements are calibrated from a separate series of absorbance measurements of samples, containing a CO_2+CO calibration mixture. The ratio of the gas mixture is known with a high certainty.

In addition to the absorbance measurement, we record an oscillogram of the voltage drop across the discharge and of the discharge current, capturing several seconds of the working state of the device. This oscillogram is used to calculate the average power introduced to the discharge, as described in section 3.2. The voltage and current measurements are performed using a high voltage differential probe (Pintek DP-30K) – figure 1(4), and a current probe (Pintek PA-699) – figure 1(5). The oscillogram is created using a digital oscilloscope (Rohde & Schwarz®RTB2004 Digital Oscilloscope) – figure 1(7). Finally, all the measurement data is digitally processed using a personal computer – figure 1(8).

2.1 Discharge configurations

Three different GD configurations were tested, namely the Non-Stabilized Gliding Discharge (NSGD), the Magnetically Stabilized Gliding Discharge (MSGD) and the Magnetically Accelerated Gliding Discharge (MAGD). These are schematically presented in figure 2. In figure 2(a), the dimensions of the separate part of the discharge device are given.

The three different configurations are tested using a single device, based on a common GD design with flat diverging electrodes. Similar devices were used in [15, 16, 18, 25]. The base of the device consists of two "knife" shaped metal electrodes, a pair of quartz glasses and several structural elements, made of various materials including teflon, aluminium and steel. We tested two types of electrodes, composed of different materials – aluminium and stainless steel (SS, ALSI 34).

For all of the discharge configurations, the plasma is confined to the volume between the electrodes, by a pair of quartz glass panels. In essence, the metal electrodes are "sandwiched" between these glasses. This ensures that a larger portion of the inlet gas interacts with the plasma, and is also crucial

for the magnetic configurations, where the quartz glasses separate the magnets from the electrodes, preventing any short circuits.

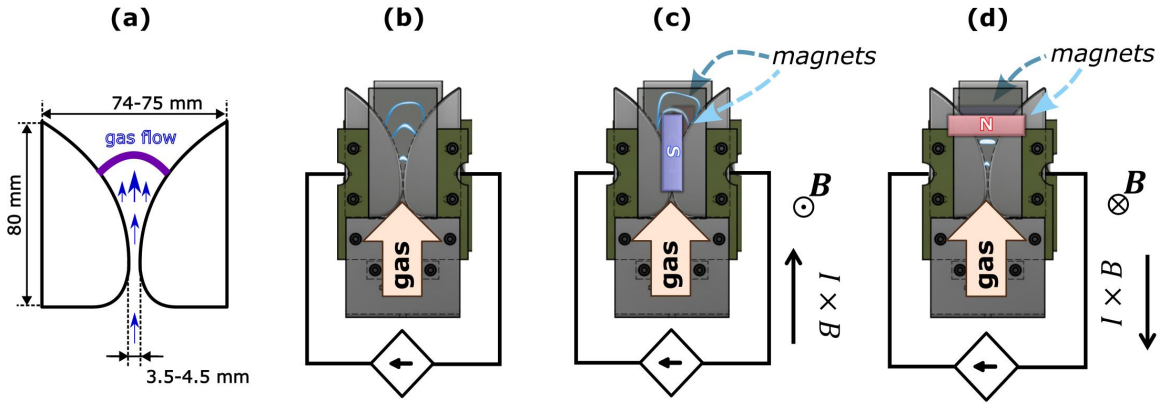

Figure 2: Dimensions of the discharge device (a), and schematics of the three types of discharge configurations – Non-stabilized gliding arc (NSGD) (b), Magnetically-Accelerated Gliding Discharge (MAGD) (c), and Magnetically-Stabilized Gliding Discharge (MSGD) (d).

All tested electrodes are 80 mm high, 35 mm wide and 3 mm thick, with identical curvatures. The closest distance between the electrodes is 3.5 mm. Each of the quartz glasses is about 2 mm thick. As illustrated in figure 2, the inlet gas is fed at the bottom side of the device, near the location of the closest separation between the electrodes. This is done from a rectangular nozzle (opening) with rounded corners, having a width of 6 mm and height of 3 mm. The 3 mm nozzle width is the same as the distance between the glasses, i.e. the width of the gas flow channel, which is also equal to the thickness of the electrodes.

For the MSGD and MAGD configurations, a pair of two permanent NbFeB magnets is placed on top of the quartz glasses, i.e there is a magnet on the outer side of each of the two quartz glasses. The two magnets are identical rectangular prisms, with dimensions 50 mm $\times$ 10 mm $\times$ 1.5 mm. They stay in place, one on each side of the device, because of their mutual attraction. The two magnets create a strong magnetic field $\approx 0.5 - 0.6$ T, in the space between the electrodes. The orientation of the magnets, relative to the electrodes, determines the direction of the magnetic force. For MAGD, the magnetic force is directed upwards (downstream), so that the gliding effect is enhanced. In the MSGD configuration, the magnetic force is directed downward, opposite the gas flow (upstream), and the arc gets stabilized at the position where the gas drag equalizes the magnetic force. The magnets are separated by a distance of 7 mm (two quartz glasses each 2 mm thick and 3 mm thick electrodes). Using the known values for the strength of the magnetic field inside the magnetic material, we calculated the magnetic field flux density distribution around the magnets, by means of magnetostatic computer simulations. The results from these calculations showed that the flux was concentrated in the space between the magnets, as one would expect. This would mean that in the actual physical device, the magnetic flux will be the highest in the region between the two electrodes. For the magnetically accelerated configuration – MAGD, the magnets are oriented vertically, as illustrated on figure 2(c). This ensures that the arc experiences the action of the magnetic field for a longer time period, during its gliding. For the stabilized MSGD setup – figure 2(d), the magnets are in a horizontal orientation, at a certain position away from the inlet nozzle. This creates a sort of a magnetic "barrier", which retards and eventually stops the motion of the arc, creating the so-called stabilized arc.

2.1.1 NSGD configuration - Non-stabilized gliding discharge

The non-stabilized configuration (NSGD) – figure 2(b), works in the classical GD (GA) regime, where the combined effect of thermal advection and gas flow drag, pushes the plasma along the electrodes, making it a gliding discharge. The discharge starts as a contracted channel at the closest separation between the electrodes and as it travels, it becomes more elongated. After a certain critical length, its voltage drop becomes too great for the power supply to maintain, so it extinguishes and reignites at the closest distance. This repetition is periodic, with a frequency determined by a multitude of factors, including the power supply.

2.1.2 MAGD configuration - Magnetically-accelerated gliding discharge

In the second configuration (MAGD) – figure 2(c), the presence of an external magnetic field produces an additional magnetic force in the direction of the flow. This increases the speed of gliding, and shortens the period between ignition and extinction. A similar type of discharge was tested in [17], where it was shown that at high enough flow rates, the effect of the magnetic force becomes insignificant, compared to the drag from the gas flow. In [17], it is further argued that this configuration increases the effective plasma volume, where the gas can be treated, and prevents the formation of cathode spots, because it pushes the arc along the electrodes faster. We expected that the additional accelerating action could potentially have a positive effect on conversion, but we were not able to observe any improvement of this configuration over the simple NSGD setup. This can be seen from the results, presented in section 4.

2.1.3 MSGD configuration - Magnetically-stabilized gliding discharge

In the third, magnetically-stabilized configuration (MSGD) – figure 2(d), a magnetic field is also applied. The orientation of the magnetic field is such that the magnetic force opposes the gas flow drag. In this way, the magnetic field stabilizes the discharge at certain place along the electrodes, where the drag from the flow becomes equal to the magnetic force. The arc remains stationary at that location with parameters which remain steady in time. Obviously, this configuration is limited to a specific maximum flow rate, after which the magnetic force is no longer capable of stabilizing the arc, because it is much smaller than the force experienced from the gas drag.

2.2 Power supply

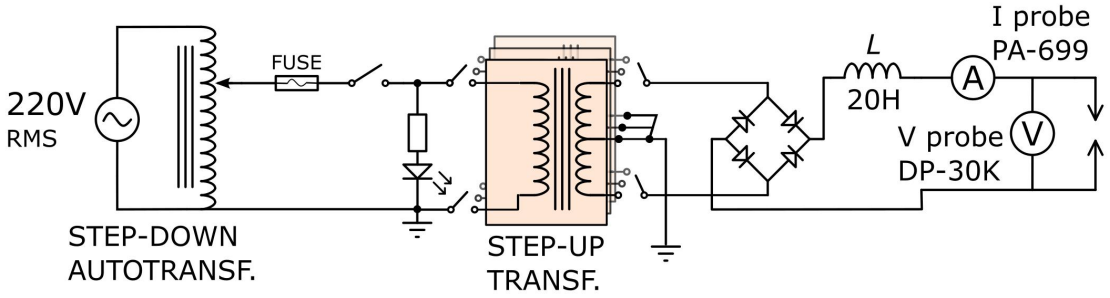

Figure 3: Electrical schematic of the high voltage power supply unit.

One of the main characteristics of the low current arc discharges studied here, is the negative dV/dI relation between the discharge current I and voltage drop V. When the capacitance of the connecting cables and the electrodes charges up to the breakdown voltage, a breakdown occurs, and the stored energy is released to form the initial conducting channel. The cable capacitance in our system is

$\approx$ 100 pF. After the breakdown, the voltage across the discharge drops by several kV, and the current simultaneously increases, until it reaches its maximum value, determined either by the power supply internal resistance or an external resistor, connected in series.

For the power supply used in our experiments, the goal was to minimize the ohmic losses. In our case the maximum discharge current is not limited by a resistor, but instead it is limited by the step-up transformer itself. A circuit schematic of the power supply is presented in figure 3. We can set the maximum discharge current by switching between one of several step-up neon transformers – SIET Metalbox 10 kV (effective AC voltage). Each transformer has a different value of its maximum secondary winding current, ranging from 25 mA to 110 mA. By connecting two of these transformers in parallel, we were able to reach currents of 210 mA as well. There is also a large inductor connected in series to the discharge. The inductor acts as a low pass filter, partially filtering the rectified voltage, after the bridge rectifier (Graetz circuit).

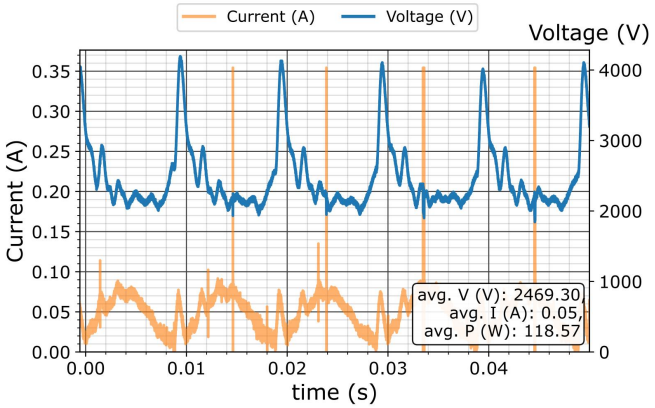

Figure 4: Typical oscillogram for the MSGD configuration. For this measurement, the maximum step-up transformer secondary current is 50 mA, and the inlet gas flow rate is 6 Ln/min.

We should point out that the current circuit is not able to supply a well rectified voltage and current, so there is still a significant AC component at 100 Hz (in our region the grid frequency is 50 Hz). This can be seen in the current and voltage signals, shown in figure 4. This can have an effect on the discharge, since it can cause periodic arc extinction, resulting from the voltage dropping to a very low value. In the future, we consider combining several step up transformers in a three-phase power supply circuit, or the use of a more sophisticated switched-mode power supply.

3 Measured quantities and their uncertainties

For this study, we measure three of the most commonly used quantities in the literature, namely the CO_2 conversion, the specific energy input (SEI), and the energy efficiency of the process. We calculate these values in an identical way to [1, 17, 18, 25] and others.

3.1 Conversion

The conversion is defined as the fraction (or percent) of converted CO_2 gas:

$$X_{CO_2}, \% = \frac{N^{\text{init}}_{CO_2} - N^{\text{final}}_{CO_2}}{N^{\text{init}}_{CO_2}} \times 100\ \% = X_{CO_2} \times 100\ \%, \tag{1}$$

where $N^{\text{init}}_{CO_2}$ is the initial concentration of CO_2 and $N^{\text{final}}_{CO_2}$ is the final concentration, after the treatment process. As already mentioned in section 2, we measure the CO_2 conversion from the relative

absorbance of a sample of the processed gas. The absorbance is measured at a single line of the CO molecule, at 2209 cm^{-1}, and it is proportional to the concentration of CO gas in the sample, which gives us the conversion percent. Therefore, we can directly relate the conversion value to the absorbance through a coefficient α, as:

$$X^0_{CO_2} = \alpha I_{\text{absorb}}, \tag{2}$$

where $X^0_{CO_2}$ is in the range $[0, 1]$. The value of α is found through a separate series of measurements, using an etalon gas mixture of 20 % CO and 80 % CO_2.

3.1.1 Gas expansion correction

In the dissociation process, the CO_2 molecule is split into a CO molecule and 1/2 of a O_2 molecule, so the conversion of CO_2 leads to an expansion of the volume by a factor of 1.5 (in case of complete conversion). In order for the measured conversion to satisfy the definition given in equation 1, we need to correct for the gas expansion. As the conversion process expands the gas, some of it escapes, because our system remains at atmospheric pressure. To find the correct value for the final CO_2 concentration – $N^{\text{final}}_{CO_2}$, we need to account for the converted gas that has already left the system.

We correct the value of the conversion in an identical way to [8, 19]. The correct concentration of CO_2 after processing, can be expressed as: $N_{CO_2} = N^{\text{init}}_{CO_2}(1 - X_{CO_2})$. During operation, the gas volume has expanded according to the law: $V_{\text{expand.}} = V_0(1.5X_{CO_2} + (1 - X_{CO_2})) = V_0(1 + 0.5X_{CO_2})$, and because the entire system is remaining at a fixed pressure (1 atm), the measured conversion of CO_2 in the FT-IR sample – $X^0_{CO_2}$, will have a larger value than the real conversion X_{CO_2}. Both of these quantities are related as:

$$X^0_{CO_2} = 1 - \frac{(1 - X_{CO_2})}{(V_{\text{expand.}}/V_0)} = 1 - \frac{(1 - X_{CO_2})}{(1 + 0.5X_{CO_2})}. \tag{3}$$

We can derive equation 3, from the relation of the concentration of CO_2 in the gas sample and the concentration of CO_2 of the entire volume of the processed gas (including that which has left the system after processing):

$$(1 - X^0_{CO_2})\frac{N^{\text{cell,init}}_{CO_2}}{V^{\text{cell}}} = (1 - X_{CO_2})\frac{N^{\text{init}}_{CO_2}}{(V_0(1 + 0.5X_{CO_2}))} = \frac{p_0}{T_0}, \tag{4}$$

where V_0 is the volume of the initial number of CO_2 molecules in the system – $N^{\text{init}}_{CO_2}$, and V^{cell} is the volume of the FT-IR gas sample cell, equal to the volume of $N^{\text{cell,init}}_{CO_2}$ molecules, contained in a gas sample with only CO_2. The pressure $p_0 = 1$ atm and T_0 is equal to room temperature. Equation 3 is found, upon substituting in $N^{\text{init}}_{CO_2}/V_0$ in equation 4, using the relation: $N^{\text{cell,init}}_{CO_2}/V^{\text{cell}} = N^{\text{init}}_{CO_2}/V_0 = p_0/T_0$, for the state of the system, when there is no conversion $X^0_{CO_2} = X_{CO_2} = 0$.

From equation 3, we can express the correct conversion value X_{CO_2}, from the one measured from the gas sample – $X^0_{CO_2}$, as:

$$X_{CO_2} = \frac{2X^0_{CO_2}}{(3 - X^0_{CO_2})}, \tag{5}$$

where it should be noted that the $X^0_{CO_2}$ value is in the range of $[0, 1]$.

3.2 Specific energy input (SEI)

The specific energy input – SEI (J/mol), is the energy delivered per mole of gas. It can be expressed from the gas flow rate and power as:

$$\text{SEI (J/mol)} = \frac{P\ \text{(J/s)}}{Q\ \text{(Ln/s)} \times (1/22.4)\ \text{(mol/Ln)}}, \tag{6}$$

where Q (Ln/s) is the gas flow rate in normal liters per second. The unit Ln is equal to 1 liter at normal conditions (0° C, 1 atm). The quantity P is the average power delivered to the discharge, during continuous operation of time T. It is calculated as:

$$P = 1/T \int_0^T U(t)I(t)\mathrm{d}t \approx 1/N \sum_{i=1}^{N} U_i I_i, \tag{7}$$

using the sample data of N values for the voltage drop U_i and the discharge current I_i, from the oscilloscope measurements. The SEI values are also commonly expressed in units of eV per molecule [1].

3.3 Energy efficiency

The energy efficiency η is given as the ratio of the minimal required energy for a conversion of $X_{\mathrm{CO_2}}$, to the total energy spent. It can be expressed through the specific energy input SEI as:

$$\eta = \frac{X_{\mathrm{CO_2}} \times \Delta H_R}{\mathrm{SEI}} \times 100\ \%, \tag{8}$$

where $\Delta H_R = 279.8 \times 10^3$ (J/mol) is the reaction enthalpy for the CO_2 splitting reaction.

3.4 Uncertainty analysis

As already mentioned in section 3.1, the value of $X^0_{\mathrm{CO_2}}$ is proportional to the absorbance $I_{\mathrm{absorb.}}$, by the coefficient α. The uncertainty in the absorbance value is calculated as the experimental standard deviation (defined in [26]) of all available absorbance measurements, for given values of the maximum discharge current and the input flow rate. For some experimental measurements, 10-12 absorbance samples were gathered, and for others 3-5. The relative uncertainty of the conversion is expressed as:

$$\left|\Delta X^0_{\mathrm{CO_2}}/X^0_{\mathrm{CO_2}}\right| \approx \left|\Delta I_{\mathrm{Absorb.}}/I_{\mathrm{Absorb.}}\right| + \left|\Delta\alpha/\alpha\right|, \tag{9}$$

Here $X^0_{\mathrm{CO_2}}$ is the value of the conversion, without the expansion correction. One can further calculate the absolute uncertainty for the actual conversion $X_{\mathrm{CO_2}}$, using the expansion correction formula (equation 5):

$$(\Delta X_{\mathrm{CO_2}})^2 = \left(\frac{dX_{\mathrm{CO_2}}}{dX^0_{\mathrm{CO_2}}}\right)^2 (\Delta X^0_{\mathrm{CO_2}})^2 = \frac{36}{(3 - X^0_{\mathrm{CO_2}})^4}(\Delta X^0_{\mathrm{CO_2}})^2. \tag{10}$$

The value for the relative uncertainty of the coefficient α is $\Delta\alpha/\alpha \approx 1$ %. It is calculated as the experimental standard deviation of several absorbance measurements, using an etalon gas with a known ratio of CO to CO_2. The relative uncertainty in the SEI (defined in equation 6) is expressed as:

$$|\Delta\mathrm{SEI}/\mathrm{SEI}| \approx |\Delta Q/Q| + |\Delta P/P| \tag{11}$$

The absolute uncertainty in the averaged power P (equation 7) is calculated as the average of the uncertainties of all momentary power measurements – $\Delta P = 1/N \sum_{i=1}^{N} \Delta P_i$. The uncertainty of the sample ΔP_i is computed from the combined standard uncertainty (see section 5.1 of [26]) of the current and voltage samples:

$$\Delta P_i^2 = \left(\frac{\partial P}{\partial U}\right)^2 \Delta U_i^2 + \left(\frac{\partial P}{\partial I}\right)^2 \Delta I_i^2 = (\Delta U^2_{\mathrm{probe}} + \Delta U^2_{\mathrm{osc.}})I_i^2 + (\Delta I^2_{\mathrm{probe}} + \Delta I^2_{\mathrm{osc.}})U_i^2. \tag{12}$$

The uncertainties in the voltage and current samples account for both the probe ($\Delta U_{\mathrm{probe}}$, $\Delta I_{\mathrm{probe}}$) and oscilloscope ($\Delta U_{\mathrm{osc.}}$, $\Delta I_{\mathrm{osc.}}$) uncertainties. The current and voltage probes have an uncertainty of $2 - 3$ %, and the oscilloscope introduces a further 1.5 %, depending on its screen range.

Lastly, the relative uncertainty in the energy efficiency is calculated as the sum:

$$|\Delta\eta/\eta| \approx |\Delta X_{\mathrm{CO_2}}/X_{\mathrm{CO_2}}| + |\Delta\mathrm{SEI}/\mathrm{SEI}| \tag{13}$$

where the uncertainty in ΔH_R is taken to be insignificant.

From the data available, we can say that the relative uncertainty in $X_{\mathrm{CO_2}}$ is in the range of $10\ \% - 12\ \%$ and the relative uncertainty for the energy efficiency η, is around $15 - 17\ \%$ of the energy efficiency value.

4 Results and discussion

We tested the three discharge types, NSGD, MAGD and MSGD for discharge current values ranging from 25 to 210 mA, at flow rates of 1 to 14 Ln/min. We also tested a modification of the NSGD discharge without quartz glasses. It is referred as NQNSGD – No Quartz Non-Stabilized Gliding Discharge.

4.1 Results for the conversion and energy efficiency

In figure 5, we present the measured conversion and energy efficiency of all the performed experiments, as a function of the power and the SEI. These results show the overall trends and include all variations of experimental conditions and discharge configurations. Regardless of the discharge type, we can see that above a SEI value of 4 kJ/Ln, the conversion remain fairly constant. The opposite is true for the energy efficiency, as it drops with increasing SEI. This is logical, because the energy efficiency is inversely proportional to the SEI (see equation 8 above). The maximum values for the conversion are around 8 %, while for the energy efficiency, there are values above 40 %. The SEI range, where both the efficiency and conversion have high values is between $2 - 4$ kJ/Ln, yielding a conversion of about $5 - 6$ %, and an energy efficiency of about $18 - 30$ %.

The recombination of CO and O back into CO_2 could be responsible for the fact that the CO_2 conversion does not rise further with rising SEI, and thus for the drop in energy efficiency due to the increased retention time at lower flow rates (corresponding to higher SEI). In [5, 24], it was suggested that further enhancement of the conversion performance can be expected by fast cooling (quenching) of the gas, immediately after it leaves the active plasma volume. This would in theory limit the recombination of CO and O back to CO_2.

From figure 6, we can see that for the NSGD configuration, at low power, the highest conversion can be achieved at the lowest gas flow rate of 2 Ln/min. The energy efficiency generally increases with the flow rate and decreases with power.

Figure 7 presents the comparison between the three different discharge types, at 100 mA current. The tendencies observed here also apply for the other current values. At flow rates above 3 Ln/min, the NSGD configuration has the highest conversion values, while the MSGD configuration has the best results for both conversion and energy efficiency below 3 Ln/min. At 100 mA current, a conversion of 6.5 % is reached, with an energy efficiency of $13 - 15$ %. Higher flow rates yield a much better energy efficiency, but for lower conversion. It was surprising that the MAGD discharge has both lower conversion and energy efficiencies, compared to the NSGD type, at these conditions. The MAGD and MSGD configurations have similar conversion values, but the efficiency tends to be higher for the MSGD setup. This is due to the higher power dissipation in the MAGD configuration, being the result of the arc elongation and higher average arc voltages.

Additional tests of the non-stabilized configuration were performed, where the side quartz glasses were removed. These tests are marked as the NQNSGD series. A comparison between the results of the non-stabilized configuration, with and without glasses is presented in figure 8. For our designs, the quartz glass plates serve two roles. One is to channel the gas flow, and the other is to separate any magnets (if present) from the electrodes. For all tested flow rates, there is a consistent relative difference for both conversion and energy efficiency. At 2 Ln/min, this difference is the largest – about

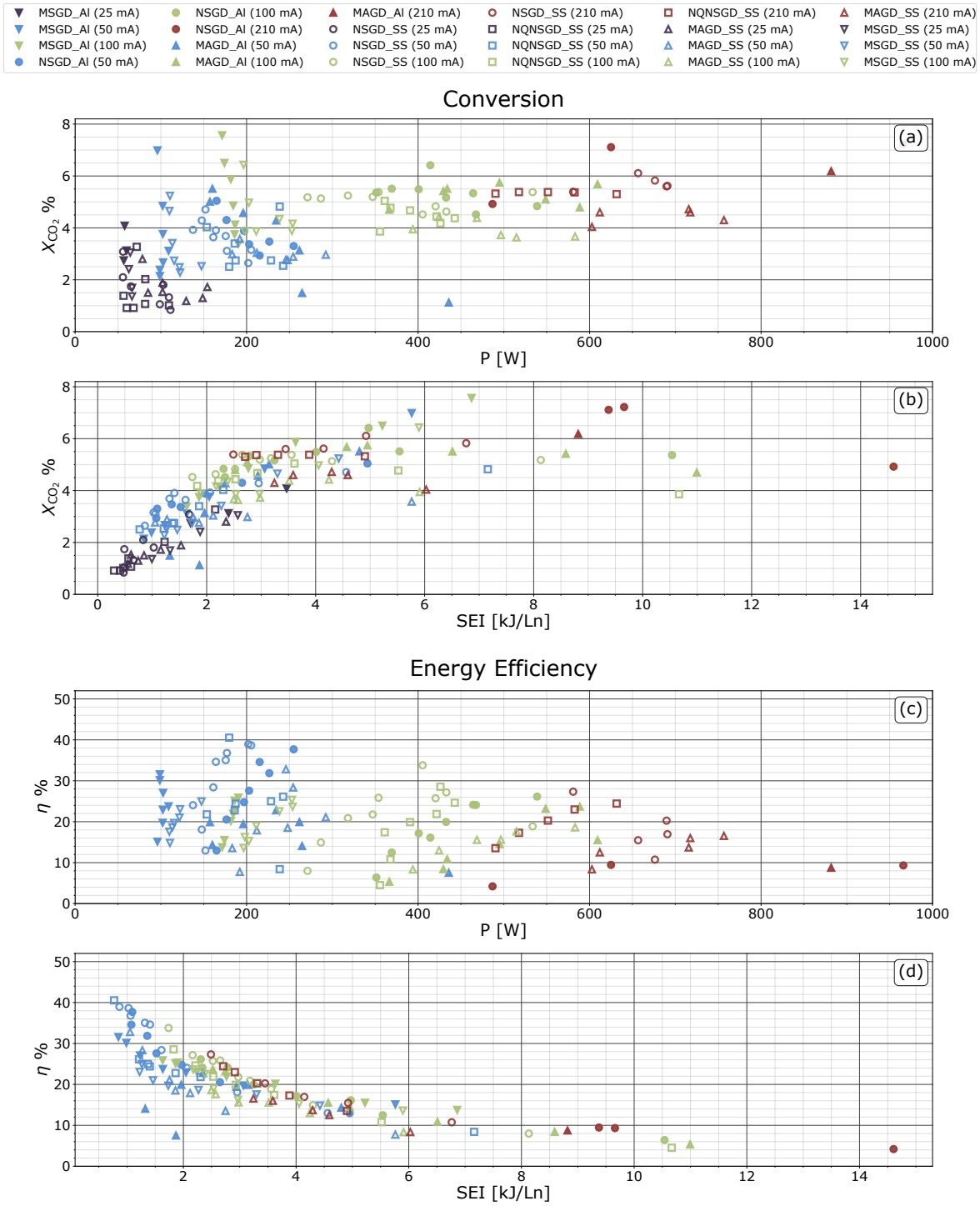

Figure 5: Measured conversion (a, b) and energy efficiency (c, d), for the three different configurations, two different electrode materials (SS – stainless steel, Al – aluminium), at different currents (as indicated in the legend), plotted as a function of the discharge power P (a, c) and SEI (b, d). Marker styles: ▼ MSGD, ● NSGD, ▲ MAGD, ■ NQNSGD, filled marker- Alluminium electrodes, empty marker - Stainless steel electrodes. Color denotes maximum discharge current value.

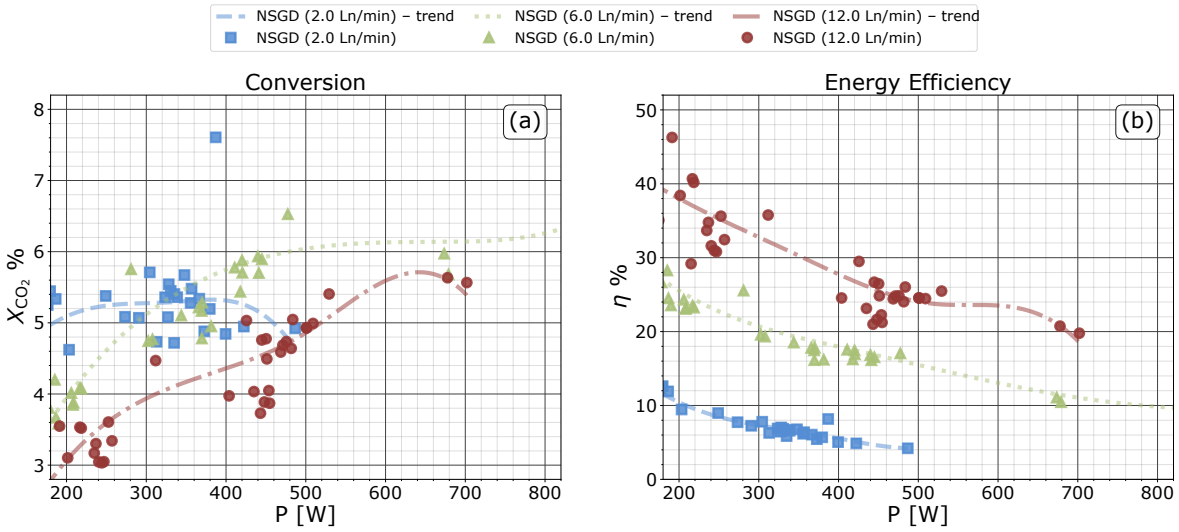

Figure 6: Conversion (a) and energy efficiency (b), given as a function of the delivered discharge power P, at three different flow rates (see legend), of the NSGD configuration for both types of electrode materials.

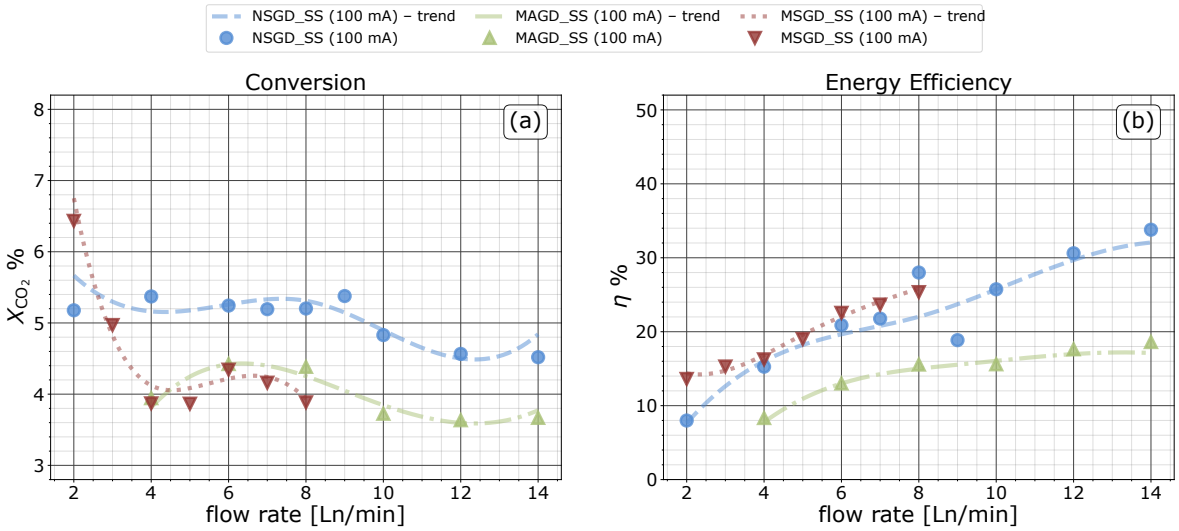

Figure 7: Comparison of the conversion (a) and energy efficiency (b) as a function of flow rate, between the three different discharge configurations, at a discharge current of 100 mA, for the stainless steel electrodes.

25 %. The probable reason for this is the enhanced gas flow expansion, in the case without glasses, at these low flow rates, which reduces the amount of treated gas. Hence, our results indicate the beneficial effect of having these side quartz glasses present in our setup.

In figure 9, a comparison is made between the measurements done with aluminium and steel electrodes, at 100 mA, for the non-stabilized NSGD configuration. The results for aluminium (Al) electrodes have comparatively higher values for the conversion, but lower for the energy efficiency. In absolute terms, the conversion is up to 1 % higher for the case of the aluminium electrodes, but only for the moderate flow rates ($4 - 10$ Ln/min). The stainless steel electrodes are better in terms of

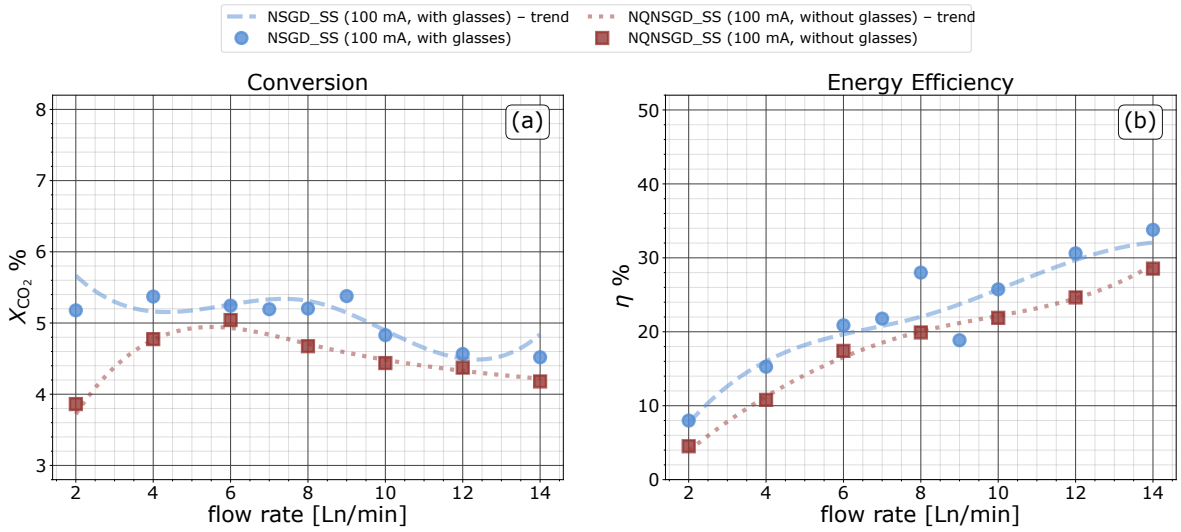

Figure 8: Comparison of the conversion (a) and energy efficiency (b) as a function of flow rate, for the NSGD configuration, with and without side quartz glass panels, at a discharge current of 100 mA.

energy efficiency, having up to 10 % higher efficiency values, for the larger flow rates. This difference can be partially explained from the fact that the Al material has higher thermal conductivity – for the Al alloy used $k_{Al} \approx 190$ $\mathrm{Wm^{-1}K^{-1}}$, and for the SS material, it is $k_{SS} \approx 14.4$ $\mathrm{Wm^{-1}K^{-1}}$ (Steel Stainless, Type 304). We argue, that the greater heat conductance of the Al material leads to an improved heat transfer away from the plasma region and the quartz glasses. This in turn could lower the gas temperature in the plasma region, which is identified to be beneficial for conversion [24].

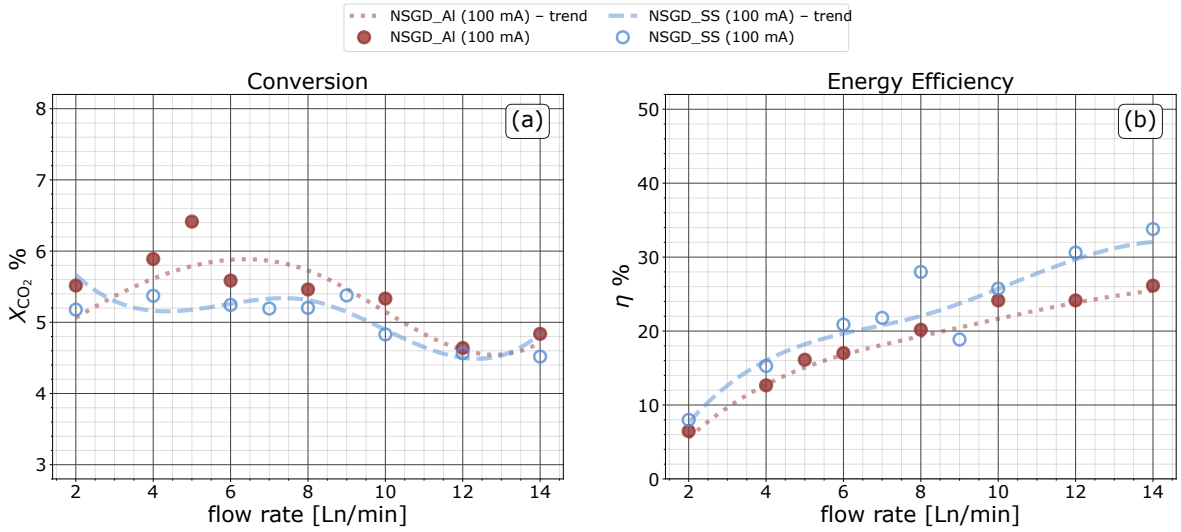

Figure 9: Comparison of the conversion (a) and energy efficiency (b), versus the flow rate, of the two different types of electrode materials used, for the NSGD configuration, at a discharge current of 100 mA.

In figure 10, the values for the conversion and energy efficiency are presented as a function of the gas flow rate. This is identical to figure 7, but for the aluminium electrodes. The value of the

discharge current is 100 mA, but the results at other currents are qualitatively the same. Generally, the conversion decreases with flow rate, for both electrode materials. For the MSGD configuration, it decreases the fastest, and after a high enough value for the flow rate, the arc can no longer be stabilized. This is the reason why we lack results for MSGD for flow rates higher than 7 Ln/min. The energy efficiency increases with flow rate, opposite to the conversion. This can again be explained from the formula of the energy efficiency (equation 8) – the SEI is inversely proportional to the flow rate (at constant power), so the energy efficiency will rise with flow rate, because the drop in conversion is not very prominent.

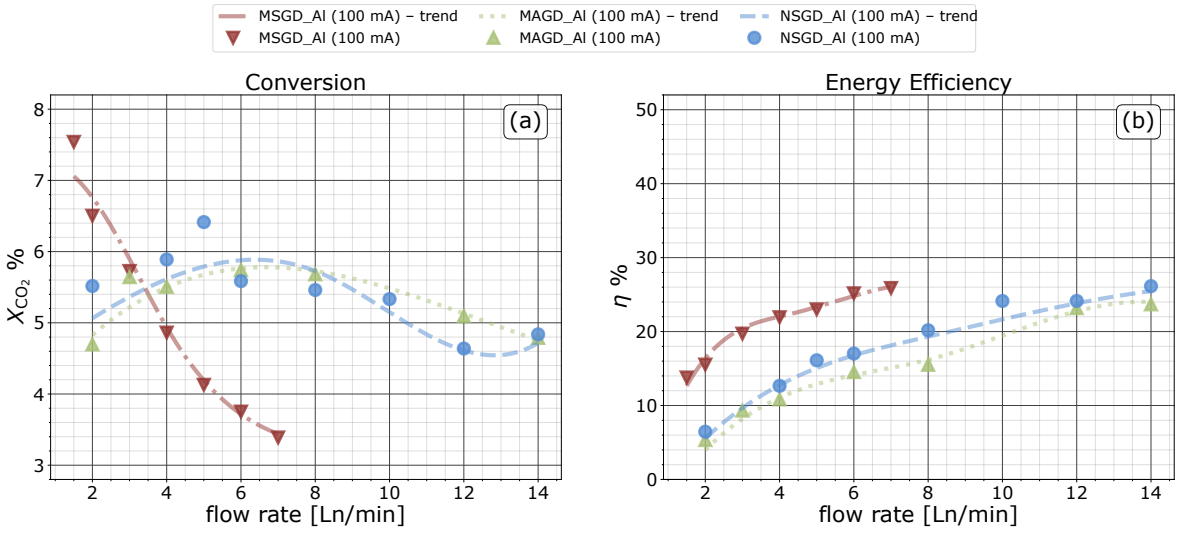

Figure 10: Conversion (a) and energy efficiency (b) at 100 mA, comparing the three different discharge configurations, as a function of flow rate, for the aluminium (Al) electrodes.

The magnetically-stabilized configuration performs similarly, regardless of the electrode material. Further, the distance between the electrodes seems to affect both the energy efficiency and conversion.

We have also studied the effect of gas heating, and how it affects the conversion as a possible way of increasing the efficiency by heat recovery from the outlet gas. Using a separate heating source, separated from the gas, we were able to raise the gas temperature to $140-170^{\circ}$ C, before it entered the plasma. The results showed that this didn't have any significant effect on conversion. This is probably because these temperatures are too small, compared to the critical temperatures of $2000-3000$ K needed for thermal dissociation.

4.2 Discharge behaviour

Here we discuss some more general observations of the discharge behaviour, which could be helpful for the explanation of the obtained results. Typically, the discharge starts when the voltage across the electrodes reaches a value above $8-10$ kV. It is ignited at the closest inter-electrode distance. As the current builds up, the voltage drops rapidly, and we can reach the maximum possible current in the secondary winding, depending on the transformer connected. In the non-stabilized and accelerated configurations (NSGD and MAGD), when the arc is formed at the closest distance, it is brighter, contracted and has a small diameter. At this stage we expect high temperature in the plasma column core, and strong contraction. Figure 11(a) shows a photo of the arc evolution in time, taken with a fast camera with exposure time of 1 μs and 2 ms periods between the consecutive photos. The left and right electrodes are the anode and cathode respectively.

At a later stage of development, the arc expands and transitions to a less contracted positive column

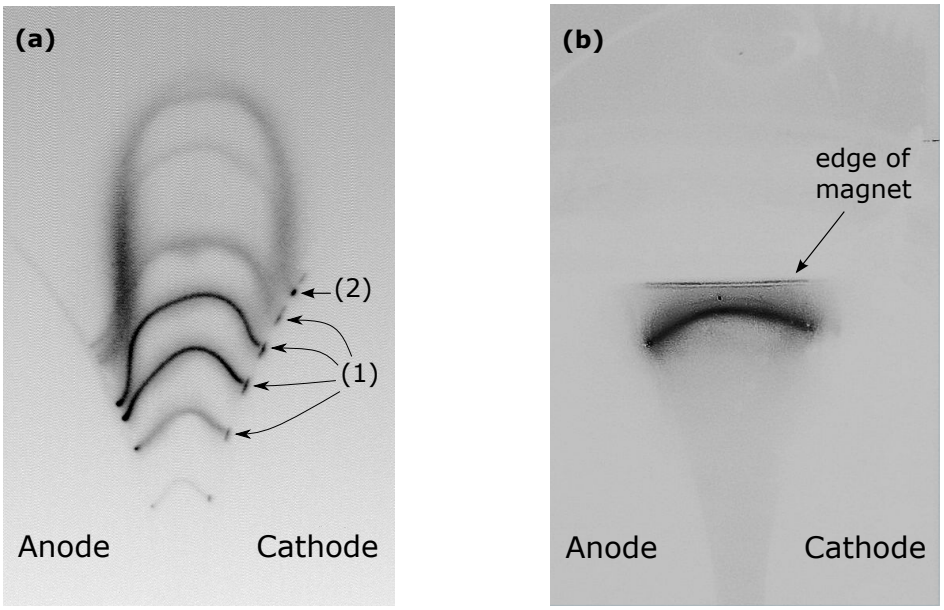

Figure 11: On subfigure (a): Combined photo (negative) of the arc evolution in time, taken with a fast I-CCD camera PI-Max with 10 expositions, 1 μs each, separated by 2 ms. The electrodes on the left and right are the anode and cathode respectively. Discharge current of 100 mA, 4 Ln/min gas flow, in the NSGD discharge configuration. Points (1) are the cathode regions of the discharge with negative glow in case of glow mode. Point (2) is a probable arc spot and a sign of transition to an arc mode. On subfigure (b): Photo (negative) of a stationary, stabilized arc in the MSGD configuration, taken with ms exposure time. The electrodes on the left and right are the anode and cathode respectively. Discharge current of 50 mA, 5 Ln/min gas flow, in the MSGD discharge configuration.

with lower light emission, which is an indication of lower gas temperature and highly non-equilibrium state. As the electrical data shows, the increase of the voltage naturally leads to a slight decrease in the current since the power source is not a perfect current source. The latter, as shown at similar conditions but in air in [27], leads to a lower gas temperature and weaker contraction.

Another important observation is the large cathode region during the gliding of the discharge downstream. This is typical for a glow discharge, sustained by secondary electron emission and the cathode region light emission is dominated by the negative glow [28]. At low current values, in the order of hundreds of mA and lower, the discharge could operate either in arc or glow regime [27, 29, 30, 31], depending on the cathode surface conditions, operating gas and discharge dynamics. The examination of several photos of the discharge shows that at 100 mA and SS electrodes, the arc is usually sustained in glow mode during the gliding and eventually transitions to an arc at certain points as in figure 11(a), point (2), where it is probably attached for longer time or the electrode has protrusions. We expect that the discharge is mainly in glow mode, and also for the lower current values of 50 and 25 mA. Note that at these currents, the negative glow region is smaller and one cannot distinguish whether the discharge is in glow or arc regime but since the glow mode is dominant at 100 mA, there is no reason to expect something else for lower currents. Similar behaviour was observed in [27, 30], which points out that at these low currents (200 mA in their study), we are in a normal glow regime, which might transition to spark and arc discharges, with the formation of filaments, at certain conditions, i.e. with contracted positive column. Moreover, in the non-stabilized configuration, we were able to observe the short-circuiting of the arc with its body, when the arc becomes over extended.

With respect to the application of CO_2 dissociation, the regime of the cathode region (glow/arc) probably plays a certain role. We can assume that the gas treatment is mainly in the positive column

due to its much larger volume. The effect of the regime is most likely a result of different total power for given current and discharge length. The glow regime has higher power because of its higher cathode fall ($200-400$ V [28]), versus the $10-20$ V for the arc regime. Assuming that the additional power in the glow regime does not contribute to the gas treatment, the glow regime is expected to have $5-10$ % lower efficiency compared to the arc, since the cathode fall is around 5 to 10 % of the total discharge voltage and thus similar percent power will be lost in the cathode region for electrode heating.

For the NSGD configuration, based on synchronous records of the discharge voltage and fast photos (100 μs), we calculated a rough estimate of the electric field in the positive column. Assuming the voltage drop at the cathode region to be around $200-400$ V (assuming a glow regime), the field is roughly in the range of $800-2600$ Vcm^{-1}. It has a clear dependence on the arc length – the field is around $2000-2600$ Vcm^{-1} at discharge length of about $10-15$ mm, around $1000-1500$ Vcm^{-1} for lengths of $15-40$ mm, and below 1000 Vcm^{-1} for lengths of $40-80$ mm. The same trend was observed in a study of a gliding arc/glow discharge at similar low currents in air [27].

In the magnetically-stabilized configuration (MSGD), the arc is clearly more stationary, with steady parameters in time. However, when the flow becomes too high, the arc gets elongated beyond the region of the strong magnetic field. Figure 11(b) shows a bright stationary arc, formed just beneath the level of the permanent magnets. The edge of the magnets is clearly visible on the photograph in figure 11(b).

Based on photographs of the MSGD configuration in operation, we measured the length of the stabilized arc in our tests to be between $12-15$ mm, depending on the location of the magnets, relative to the electrodes. The diameter of the (visual) light emitting part of the arc was measured to be between $1-2$ mm, and to increase with the current. Because at these currents (~ 100 mA), the arc diameter is smaller than the gap between the quartz glasses (equal to the electrode width of 3 mm), the arc is pushed near one of the side walls. This behaviour was predicted in [22].

The main advantage of the MSGD configuration is that it can produce localized stationary discharges, with steady parameters. Because we observed quartz glass melting, we can conclude that the thermal portion of the stabilized arc has reached temperatures above 1000 K. This suggests a high gas temperature in the arc region, which has some effect on conversion, but we will note that the conversion also depends on the electron temperature and density, and on the gas retention time in the plasma (which can be defined by the relative difference between arc movement speed and the gas flow velocity). The disadvantages of the MSGD setup also result from the fact, that the arc introduces a lot of heat. This leads to wear of the quartz glasses, and at certain conditions can even melt them, forming channels on the glass surface. The arc is localized near the magnets. This can be seen in the photograph, in figure 11(b). The heat from the arc can also cause a reduction in the magnetization of the permanent magnets. For this latter reason, we have additionally added a water cooling system to the external magnets, so that their temperature remains under the maximum rated operating temperature ($\approx 150^\circ$ C for the magnets used).

From the arc length, at the position where it is magnetically-stabilized, and the calculated values of the average voltage drops, ranging from 1.8 kV for the 100 mA maximum current, to 2.4 kV for 25 mA current, we calculated a rough estimate of the electric field in the positive column of the stabilized arc. Assuming the voltage drop at the cathode region to be below 20 V (arc regime), the electric field is roughly in the range of $1200-1800$ Vcm^{-1}, which is in the same order of magnitude as for the non-stabilized discharges with similar length. The regime of the cathode region (arc/glow) in this case is not clear, but due to the very high luminosity of the cathode region (spot) at 100 mA, compared to the positive column, we expect that it is in arc regime. For the lower current cases we are not able to make any conclusions.

From the typical values of the arc diameter, we can roughly estimate the average current density in the arc. Using the calculated values for the average currents, we calculated that the average current density in the light emitting portion of the positive column of the arc to be in the range of $2-4$ Acm^{-2}, depending on the transformer used, i.e. the maximum allowed discharge current.

5 Conclusions

We evaluated three types of gliding arc discharges for plasma-based CO_2 dissociation. A comparison between the three is made, based on the main performance characteristics – the conversion and the energy efficiency.

The simplest classical non-stabilized (NSGD) configuration shows the best results, for a wide range of gas flow rates. The magnetically-accelerated (MAGD) configuration surprisingly didn't perform better than the NSGD one, but overall both configurations have similar performance. The magnetically-stabilized (MSGD) setup exhibits good conversion and energy efficiency at low gas flow rates, but these drop quickly as the flow rate is increased, and for flow rates above $7 - 9$ Ln/min, the arcs can no longer be magnetically-stabilized.

We also demonstrated, that the presence of additional quartz glass plates, has a positive effect on the conversion and energy efficiency. The performance also depends on the type of electrode material. Aluminium electrodes had better conversions than stainless steel, with a relative difference of about 10 %, but the stainless steel electrodes had higher values for the energy efficiency. We argue that in the case of the aluminium electrodes, the gas temperature in the region near the plasma, can be maintained relatively lower, because of the higher thermal conductivity of aluminium, as compared to the stainless steel alloy. This could possibly explain the higher conversion values in the case of aluminium electrodes.

In general, despite the differences in the discharge configurations, the results for the CO_2 conversion and the energy efficiency follow a similar trend as a function of the SEI, showing the importance of this parameter.

The study shows that at the conditions of low current discharges, up to 200 mA, in the non-stabilized configurations, the discharge is sustained either in a glow, or in an arc regime, with dominant glow. The operation in glow regime could lead to slightly reduced efficiency compared to the arc regime, due to the considerable cathode fall and thus additional power losses for gas and cathode heating at the cathode surface. This points to a possible path for the efficiency improvement by enforcing an arc mode of the discharge.

The 2D configurations constructed and used here, allow the comparison of various modifications, including a magnetically stabilized discharge in cross gas flow. The latter was successfully tested and compared to the classical configurations of the discharge with and without quartz walls, as well as to a magnetically-accelerated discharge. The magnetically-stabilized configuration shows good performance for both conversion and energy efficiency, at low gas flow rates.

Acknowledgments

The authors would like to thank Prof. Dr. Khristo Tarnev for his overall participation in this project, and especially for his assistance in the experimental work with the ICCD-camera, used to capture the images of the discharge with microsecond exposure times.

Funding

This work was supported by the Bulgarian National Science Fund, Ministry of Education and Science, research grant KP-06-OPR 04/4 from 14.12.2018 and by the European Regional Development Fund within the Operational Programme "Science and Education for Smart Growth 2014 - 2020" under the Project CoE "National center of mechatronics and clean technologies" BG05M2OP001 − 1.001 − 0008.

Data Availability

All data related to this article can be obtained from the authors, upon request.

References

[1] R. Snoeckx, A. Bogaerts, Plasma technology – a novel solution for CO2 conversion?, Chem. Soc. Rev. 46 (2017) 5805–5863. https://doi.org/10.1039/c6cs00066e.

[2] M. Mikkelsen, M. Jorgensen, F.C. Krebs, The teraton challenge. A review of fixation and transformation of carbon dioxide, Energy Environ. Sci. 3 (2010) 43–81. https://doi.org/10.1039/b912904a.

[3] A. Berthelot, A. Bogaerts, Modeling of plasma-based CO2 conversion: lumping of the vibrational levels, Plasma Sources Sci. Technol. 25 (2016) 045022. https://doi.org/10.1088/0963-0252/25/4/045022.

[4] T. Kozak, A. Bogaerts, Evaluation of the energy efficiency of CO2 conversion in microwave discharges using a reaction kinetics model, Plasma Sources Sci. Technol. 24 (2014) 015024. https://doi.org/10.1088/0963-0252/24/1/015024.

[5] A. Fridman, Plasma Chemistry, Cambridge University Press, 2008, p. 259-268

[6] A. Bogaerts, G. Centi, Plasma Technology for CO2 Conversion: A Personal Perspective on Prospects and Gaps, Front. Energy Res. 8 (2020). https://doi.org/10.3389/fenrg.2020.00111.

[7] R. Aerts, W. Somers, A. Bogaerts, Carbon Dioxide Splitting in a Dielectric Barrier Discharge Plasma: A Combined Experimental and Computational Study, ChemSusChem. 8 (2015) 702–716. https://doi.org/10.1002/cssc.201402818.

[8] R. Snoeckx, S. Heijkers, K. Van Wesenbeeck, S. Lenaerts, A. Bogaerts, CO2 conversion in a dielectric barrier discharge plasma: N2 in the mix as a helping hand or problematic impurity?, Energy Environ. Sci. 9 (2016) 999–1011. https://doi.org/10.1039/c5ee03304g.

[9] D. Mei, X. Tu, Conversion of CO2 in a cylindrical dielectric barrier discharge reactor: Effects of plasma processing parameters and reactor design, Journal of CO2 Utilization. 19 (2017) 68–78. https://doi.org/10.1016/j.jcou.2017.02.015.

[10] M. Ramakers, I. Michielsen, R. Aerts, V. Meynen, A. Bogaerts, Effect of Argon or Helium on the CO2 Conversion in a Dielectric Barrier Discharge, Plasma Process. Polym. 12 (2015) 755–763. https://doi.org/10.1002/ppap.201400213.

[11] G.J. van Rooij, D.C.M. van den Bekerom, N. den Harder, T. Minea, G. Berden, W.A. Bongers, R. Engeln, M.F. Graswinckel, E. Zoethout, M.C.M. van de Sanden, Taming microwave plasma to beat thermodynamics in CO2 dissociation, Faraday Discuss. 183 (2015) 233–248. https://doi.org/10.1039/c5fd00045a.

[12] W. Bongers, H. Bouwmeester, B. Wolf, F. Peeters, S. Welzel, D. van den Bekerom, N. den Harder, A. Goede, M. Graswinckel, P.W. Groen, J. Kopecki, M. Leins, G. van Rooij, A. Schulz, M. Walker, R. van de Sanden, Plasma-driven dissociation of CO2 for fuel synthesis, Plasma Process Polym. 14 (2016) 1600126. https://doi.org/10.1002/ppap.201600126.

[13] C.M. Mitsingas, R. Rajasegar, S. Hammack, H. Do, T. Lee, High Energy Efficiency Plasma Conversion of CO2 at Atmospheric Pressure Using a Direct-Coupled Microwave Plasma System, IEEE Trans. Plasma Sci. 44 (2016) 651–656. https://doi.org/10.1109/tps.2016.2531641.

[14] M. Tsuji, T. Tanoue, K. Nakano, Y. Nishimura, Decomposition of CO2 into CO and O in a Microwave-Excited Discharge Flow of CO2/He or CO2/Ar Mixtures, Chem. Lett. 30 (2001) 22–23. https://doi.org/10.1246/cl.2001.22.

[15] A. Indarto, D.R. Yang, J.-W. Choi, H. Lee, H.K. Song, Gliding arc plasma processing of CO2 conversion, Journal of Hazardous Materials. 146 (2007) 309–315. https://doi.org/10.1016/j.jhazmat.2006.12.023.

[16] W. Wang, D. Mei, X. Tu, A. Bogaerts, Gliding arc plasma for CO2 conversion: Better insights by a combined experimental and modelling approach, Chemical Engineering Journal. 330 (2017) 11–25. https://doi.org/10.1016/j.cej.2017.07.133.

[17] L. Li, H. Zhang, X. Li, J. Huang, X. Kong, R. Xu, X. Tu, Magnetically enhanced gliding arc discharge for CO2 activation, Journal of CO2 Utilization. 35 (2020) 28–37. https://doi.org/10.1016/j.jcou.2019.08.021.

[18] H. Zhang, L. Li, X. Li, W. Wang, J. Yan, X. Tu, Warm plasma activation of CO2 in a rotating gliding arc discharge reactor, Journal of CO2 Utilization. 27 (2018) 472–479. https://doi.org/10.1016/j.jcou.2018.08.020.

[19] M. Ramakers, G. Trenchev, S. Heijkers, W. Wang, A. Bogaerts, Gliding Arc Plasmatron: Providing an Alternative Method for Carbon Dioxide Conversion, ChemSusChem. 10 (2017) 2642–2652. https://doi.org/10.1002/cssc.201700589.

[20] J.-L. Liu, H.-W. Park, W.-J. Chung, D.-W. Park, High-Efficient Conversion of CO2 in AC-Pulsed Tornado Gliding Arc Plasma, Plasma Chem Plasma Process. 36 (2015) 437–449. https://doi.org/10.1007/s11090-015-9649-2.

[21] T. Nunnally, K. Gutsol, A. Rabinovich, A. Fridman, A. Gutsol, A. Kemoun, Dissociation of CO2 in a low current gliding arc plasmatron, J. Phys. D: Appl. Phys. 44 (2011) 274009. https://doi.org/10.1088/0022-3727/44/27/274009.

[22] V. Ivanov, T. Paunska, K. Tarnev, S. Kolev, Magnetic field stabilization of low current DC arc discharge in cross flow in argon gas at atmospheric pressure — a numerical modelling study, Plasma Sources Sci. Technol. 30 (2021) 085007. https://doi.org/10.1088/1361-6595/ac14a8.

[23] B.L.M. Klarenaar, R. Engeln, D.C.M. van den Bekerom, M.C.M. van de Sanden, A.S. Morillo-Candas, O. Guaitella, Time evolution of vibrational temperatures in a CO2 glow discharge measured with infrared absorption spectroscopy, Plasma Sources Sci. Technol. 26 (2017) 115008. https://doi.org/10.1088/1361-6595/aa902e.

[24] S.R. Sun, H.X. Wang, D.H. Mei, X. Tu, A. Bogaerts, CO 2 conversion in a gliding arc plasma: Performance improvement based on chemical reaction modeling, Journal of CO2 Utilization. 17 (2017) 220–234. https://doi.org/10.1016/j.jcou.2016.12.009.

[25] S.C. Kim, M.S. Lim, Y.N. Chun, Reduction Characteristics of Carbon Dioxide Using a Plasmatron, Plasma Chem Plasma Process. 34 (2013) 125–143. https://doi.org/10.1007/s11090-013-9499-8.

[26] BIPM, IEC, IFCC, ILAC, ISO, IUPAC, IUPAP, OIML, Evaluation of measurement data – Guide to the expression of uncertainty in measurement, JCGM 100, 2008

[27] Y.D. Korolev, O.B. Frants, N.V. Landl, V.G. Geyman, A.I. Suslov, Parameters of a positive column in a gliding glow discharge in air, Physics of Plasmas. 24 (2017) 103526. https://doi.org/10.1063/1.5003141.

[28] Y. Raizer, Gas Discharge Physics, Springer-Verlag, 1991, p. 182

[29] Y.D. Korolev, O.B. Frants, V.G. Geyman, N.V. Landl, V.S. Kasyanov, Low-Current "Gliding Arc" in an Air Flow, IEEE Trans. Plasma Sci. 39 (2011) 3319–3325. https://doi.org/10.1109/tps.2011.2151885.

[30] Y.D. Korolev, O.B. Frants, N.V. Landl, A.V. Bolotov, V.O. Nekhoroshev, Features of a near-cathode region in a gliding arc discharge in air flow, Plasma Sources Sci. Technol. 23 (2014) 054016. https://doi.org/10.1088/0963-0252/23/5/054016.

[31] S. Kolev, A. Bogaerts, Similarities and differences between gliding glow and gliding arc discharges, Plasma Sources Sci. Technol. 24 (2015) 065023. https://doi.org/10.1088/0963-0252/24/6/065023.